Chapter 3

Mathematical modelling of the dispersive mixing

Dispersive mixing of carbon black agglomerates is mainly governed by erosion and rupture mechanisms. Here, we develop a model to predict the evolution of agglomerates size during the mixing in taken into account both mechanisms. As the number of agglomerates is very large, we cannot calculate the evolution of each agglomerate one by one. We therefore use a continuous mass density distribution based on a sample averaging approach to represent the distribution of agglomerates in rubber. The evolution of such a distribution will be given by a new dispersive model that is based on transfer function. On one hand, the discrete reccurrence equation associated to this model is determined by discretizing the space size of the agglomerates in several classes. On the other hand, a family of continuous dispersive analytical models is determined from the kinetic laws presented previously. With these models, we are able to predict the evolution of any mass density distributions by solving a simple analytical equation. In a sensitivity analysis, we compare the evolution of a given size of agglomerates predicted by every model. Numerical results obtained with these models are also compared to experimental results obtained by mixing rubber with carbon black agglomerates in Mooney rheometer.

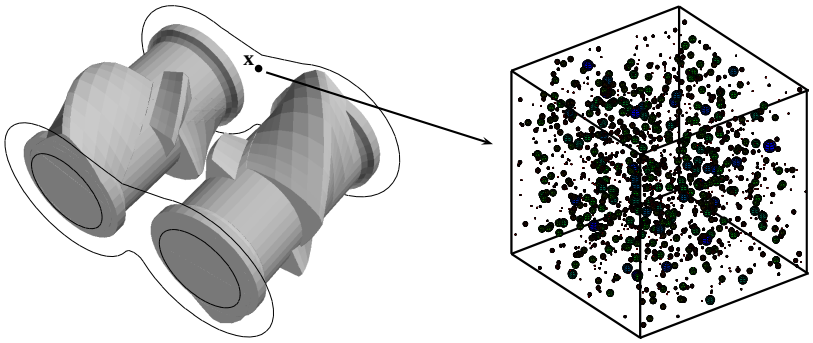

Figure 3.1: The small volume V^{repr} centered at the point **x** in the mixer chamber.

3.1 A micro-macro representation of agglomerates

Let us consider a small volume V^{repr}, called representative volume, that only contains rubber. Dimensions of this volume, centered at **x** in the mixer chamber, are on the order of $1\,\mu m$. Molecular weight of the styrene-co-butadiene rubber is equal to $210000\,\frac{g}{mol}$, where a mole contains roughly $6\,.\,10^{23}$ molecules (Avogadro's number). With the density of the styrene-co-butadiene $938\,\frac{kg}{m^3}$, this volume contains roughtly $2.78\,.\,10^{6}$ molecules. This number leads to the usual continuum assumption. In other words, it is extremely accurate to characterize this volume of rubber as macroscopically small yet microscopically large. The macroscopically small characterization is warranted since such volume has near a uniform set of thermodynamics properties (temperature, density, ect.). The microscopically large characterization warrants treating the fluid as a mathematical continuum. This assumption is acceptable because the flow in the whole mixer chamber is not dependent on the discrete nature of molecules. Consequently, limits can be taken as volume goes to zero when formulating the differential laws of the fluid motion. This proposition is known as the continuum hypothesis (Grieffies,2004) (Roberts,1994).

Continuum fluid equations are in principle related to more fundamental equations of motion through a series of averaging operations. Those fundamental equations describe the multitude of molecular degrees of freedom. Laws of continuum dynamics therefore represent a mean field theory. Huang proved this statement for the simplest gaseous system (Huang,1987). Moreover, high degree of success of such an approach

is also an evidence of its validity. From the continuum hypothesis and by applying the basic ideas from Newtonian dynamics and thermodynamics to a collection of local thermodynamically equilibrated volumes, differential laws of hydrodynamics and thermodynamics can be derived. Large spectrum of fluid motion, with spatial scale reaching from the volume to those relevant for global dynamics, can be studied from the information contained in the resulting field equations and this for temporal scales on the order of milliseconds to millennia. The efficiency of the continuum equations, for Newtonian fluids, called Navier-Stokes equations, in describing the fluid flow is very well established in the literature. As written by Griffies (2004), "That these equations are relevant over such a large space-time range represents a spectacular success in providing a rational mathematical description of natural phenomena".

According to the same approach, we can now define different size scales associated with the distribution of carbon black agglomerates. With respect to previous case, those scales are shifted to larger dimensions. We now consider a representative volume with dimensions on the order of $1\,mm$ and centered at $\mathbf{x}$ in mixer chamber (Figure 3.1). If volume fraction of carbon black in rubber is equal to 20%, a volume V^{repr} of $1\,mm^3$ contains around 382 agglomerates with a size of $50\,\mu m$. This number of agglomerates increases in time, due to dispersion, to quickly reach the number of 3056 agglomerates if the agglomerate size decreases until $25\,\mu m$. Such a number suggests that the mass of carbon black contained in the representative volume V^{repr} can be regarded as being spread uniformly over the volume V^{repr} instead of being concentrated in each agglomerate contained in V^{repr}. This volume can be considered as macroscopically small yet microscopically large with respect to agglomerate dimension.

Suppose that we wish to measure the mass density of carbon black at a point $\mathbf{x}$ located in the gap between the tip of the wing and the wall chambers at time t. Mass density of carbon black at $\mathbf{x}$ is calculated by measuring the mass of agglomerates contained in the representative volume V^{repr} centered at $\mathbf{x}$. The mass density of carbon black in V^{repr} is given by :

$$\rho(L,\mathbf{x},t) \;=\; \frac{m(L,\mathbf{x},t)}{V^{repr}(L)}$$

where ρ is the mass density, $V^{repr}(L)$ is a box with edges of size L and m is the mass of carbon black contained in this volume. Mass density in $\mathbf{x}$ depends on the size of V^{repr}. We show in Figure 3.2 qualitative evolution of the mass density as a function of the edge size L of V^{repr}. Three regions are distinguished on this plot : a region A where the evolution of ρ is governed by the chance to have a small or a high number of agglomerates in the box; a region B where mass density is approximatively constant and a region C where mass density decreases smoothly due to macroscopic heterogeneity. If the box is too large, heterogeneity of the agglomerates distribution in rubber can modify the carbon black mass contained in the box. Moreover, a part of the volume V^{repr} can be filled by one rotor and not by the mix carbon black - rubber.

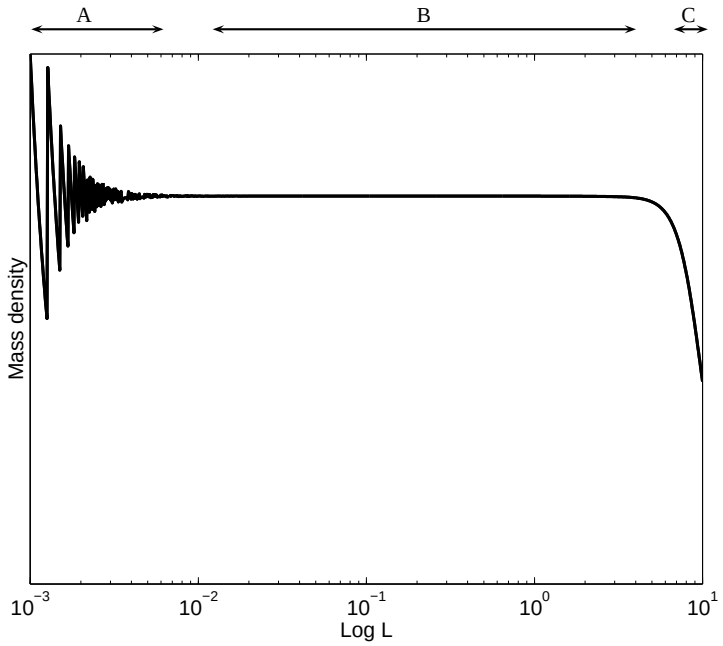

Figure 3.2: The evolution of the mass density ρ versus the size of the edges L.

In this last case, the mass of carbon black in V^{repr} is constant, but the volume of V^{repr} increases. These three regions show the same kind of separation scales than the usual continuum assumption where molecular and macroscopic scales can be identified.

Three size scales, shown in Figure 3.3, can be associated with those regions :

- an *agglomerate scale* (region A) that corresponds to the agglomerates size (lower than $10^{-2}\,mm$),
- an *intermediate scale* (region B) that corresponds to the box size where the agglomerates size distribution is viewed as a continuous field in the interval $[10^{-2}, 10]\,mm$,
- a *macroscopic scale* (region C) that corresponds to the size of the mixer. Such a scale is represented by the size of the gap between the tip of the wings of the rotors and the wall of the mixer chamber, typically $10\,mm$.

Finally, density of the continuum at the position $\mathbf{x}$ and at time t is assigned to the value

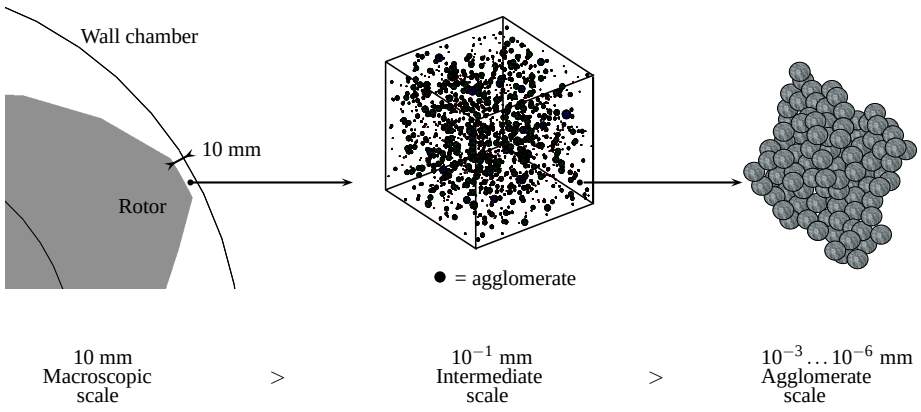

Figure 3.3: The different size scales considered in our modelling approach.

of the mass density of intermediate scale extrapolated to zero length. The mathematical point $\mathbf{x}$ is therefore assumed to be slightly smaller than macroscopic variations and bigger than microscopic fluctuations in continuum mechanics. Now, we have two scales separations. On one hand, the first separation occurs between macroscopic and agglomerate scales for the description of agglomerates distribution that will be viewed as a continuum. On the other hand, we will observe again a separation between molecular and continuous scales within the agglomerate scale domain.

From this observation, it is clear that we cannot define, in real world, the density when the size of the volume V^{repr} tends to zero. However, considering sample averaging or just imposing that such a limit is defined by using an extrapolation procedure for the intermediate scales where $\rho(L,\mathbf{x},t)$ is basically constant, it is possible to define a mass density agglomerate of size r_i in any point of the mixer $\mathbf{x}$ at time t as follows :

$$\rho_i(\mathbf{x},t) \;=\; \frac{M_i^{repr}(\mathbf{x},t)}{V^{repr}}, \tag{3.1}$$

where V^{repr} is a typical representative volume. In the virtual continuous mathematical world (that does not correspond to the reality), we use the purely mathematical limits,

$$\rho_i(\mathbf{x},t) \;=\; \lim_{V^{repr}\to 0} \frac{M_i^{repr}(\mathbf{x},t)}{V^{repr}}, \tag{3.2}$$

where M_i^{repr} is the mass of agglomerates of size r_i contained in V^{repr}. If we replace agglomerates mass M_i^{repr} by a continuous mass distribution function $m(r,\mathbf{x},t)$, which

provides the agglomerates mass of size r in V^{repr}, we then obtain a continuous mass density distribution :

$$\rho(r,\mathbf{x},t) \;=\; \lim_{V^{repr}\to 0} \frac{m(r,\mathbf{x},t)}{V^{repr}}, \tag{3.3}$$

This distribution provides the mass density of any size of agglomerates at position $\mathbf{x}$ and at time t. The evolution of the mass density distribution is governed by the usual mass transfer theory. The governing equation reads :

$$\frac{D\rho}{Dt} \;=\; -\nabla\cdot\mathbf{j} + w, \tag{3.4}$$

where w is the term of production and destruction of mass density due to dispersion process, $\mathbf{j}$ is the spatial flux of mass density and D/Dt is material derivative. In order to close this set of equations, we define a new constitutive equation for w. If we consider the initial mass density distribution illustrated in Figure 3.4, dispersion of the agglomerates of size r (in gray) implies a transfer of mass density from r to smaller sizes. In the same time, dispersion of the agglomerates of size s, in blue in Figure 3.4, also implies a transfer of mass density from the size s to smaller sizes and therefore to the size r. To model those mechanisms, the constitutive equation w, defined for a given size r, is composed of two terms : a term of production of mass density and a term of loss of mass density. This equation reads :

$$w \;=\; \underbrace{\int_\Omega G(s,r,\mathbf{x})\,\rho(s)\,ds}_{Term\ of\ production} \;\underbrace{-\rho(r)\int_\Omega G(r,s,\mathbf{x})\,ds}_{Term\ of\ loss},$$

where $G(r,s,x)$ is the function that provides the rate of transfer of mass density from size r to any size s and Ω is the space of agglomerates size.

Rate of transfer of mass density from the class r to the class s depends on the mechanism of dispersion, on the size r and on the shear rate. We here assume that the transfer function $G(r,s,x)$ is obtained by linear combination of two independent functions $G_{erosion}$ and $G_{rupture}$ that respectively model rupture and erosion mechanisms. Obviously, it is a strong assumption but this approach is quite attractive because it is very simple and it models correctly the dispersion when only the erosion mechanism or the rupture mechanism is observed. Nevertheless, we are not able to prove that linear combination of transfer functions is the most efficient way to model dispersion when both mechanisms are observed simultaneously. Functions $G_{erosion}$ and $G_{rupture}$ are determined by multiplying two parent transfer functions,$\hat{G}_{erosion}$ and $\hat{G}_{rupture}$, by two independent functions, k and l, that take into account the dependence of erosion and rupture mechanisms on the agglomerates size and on shear rate respectively. Those functions modify the amplitude of parent transfer functions to obtain a better prediction of both mechanisms. The shape of the functions k, l, $\hat{G}_{erosion}$ and $\hat{G}_{rupture}$ is arbitrary. Typical shape of parent transfer functions for erosion and rupture are illustrated in Figure 3.5. Parent transfer function for erosion is composed of two peaks.

The peak centered at the size r models the transfer of mass density from r to the sizes s, close to r, due to the removal of small fragments at the surface of the agglomerates of size r. The second peak, located in the smallest sizes, models the increase of mass density of these small fragments. Parent transfer function for rupture is only composed of one peak centered at an intermediate size. This peak models the transfer of mass density from r to several sizes of agglomerates due to rupture mechanism. Final transfer function $G(r,s)$ is then given by :

$$\begin{aligned} G(r,s) &= k_{erosion}(r)\, l_{erosion}(\dot{\gamma})\, \hat{G}_{erosion}(r,s) \\ &\quad + k_{rupture}(r)\, l_{rupture}(\dot{\gamma})\, \hat{G}_{rupture}(r,s) \end{aligned}$$

The spatial flux of mass $\mathbf{j}$ is modelled by the Fick's law but we neglect it because it is a very slow process with respect to the transfer rate of mass density from size r to any size s. The Fick's law assumes that flux of mass is proportional to the gradient of mass density in the flow. This law reads :

$$\mathbf{j} = -D\nabla\rho(r),$$

where D is the spatial mass diffusion coefficient. Finally, the model can be written as :

$$\frac{D\rho}{Dt} = -\nabla\cdot(D\nabla\rho(r)) + \int_\Omega G(s,r,\mathbf{x})\,\rho(s)\,ds - \rho(r)\int_\Omega G(r,s,\mathbf{x})\,ds, \qquad (3.5)$$

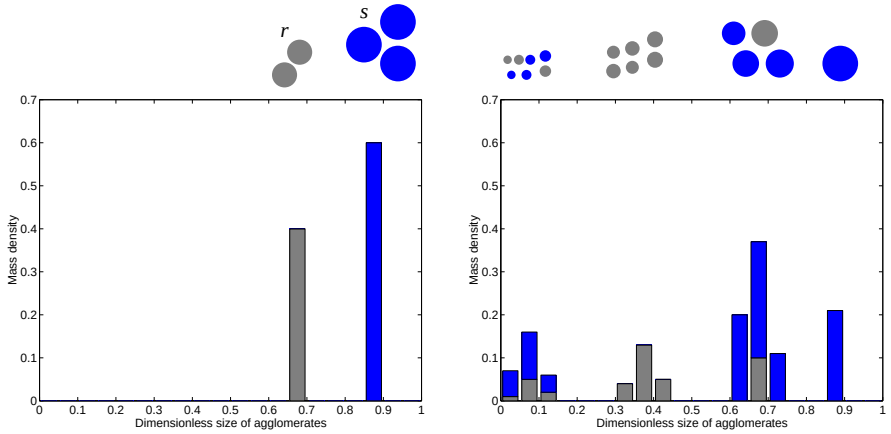

(a) (b)

Figure 3.4: Dispersion mechanism implies a transfer of mass density from the size s and r to a set of sizes. Transfer of mass density can be observed from the size s to the size r.

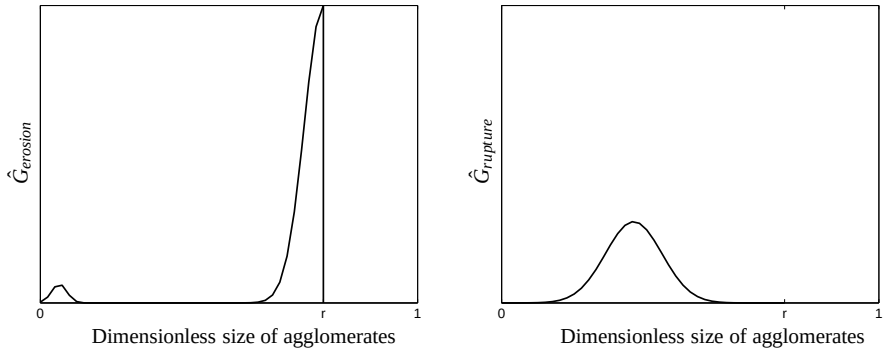

Figure 3.5: Typical shape of the parent transfer functions for (a) the erosion mechanism and (b) the rupture mechanism of agglomerates of size r.

An efficient way to solve such an equation is to adopt a Lagrangian approach where the Fick's law is neglected. In fact in most application considered in this work, the effects of rupture and erosion are quite larger than the Fick's diffusion. However, if we adopt an Eulerian numerical scheme, the Fick's diffusion can be easily incorporated and is, in general, suitable for numerical purposes.

In a Lagrangian framework when the Fick's diffusion is neglected, the equation 3.5 becomes :

$$\frac{\partial \rho(r)}{\partial t} = \int_{\Omega} G(s,r)\, \rho(s)\, ds - \rho(r) \int_{\Omega} G(r,s)\, ds, \tag{3.6}$$

In order to better understand the dynamics of our models, we discretize the continuum mass density distribution in several classes. The transfer function G then becomes transfer matrix. Each term of this matrix governs the transfer of mass density between each class. Such an approach allows us to investigate in details the effect of the shape of the transfer matrix on the evolution of the mass fraction distribution. In the next section, we propose two kinds of matrix that respectively reproduce the effect of erosion and rupture mechanisms on the mass density distribution.

3.2 A discrete recurrence equation

If we discretize mass density distribution in several classes C_i (with $i = 1 \dots n$) characterized by a typical size r_i, the discrete recurrence equation associated to the equation 3.6 is the following :

$$\frac{\partial \rho_i}{\partial t} = \sum_{j=1}^{n} G_{ij}\, \rho_j - \rho_i \sum_{j=1}^{n} G_{ji}. \tag{3.7}$$

where G_{ij} is the transfer rate of mass density from class C_j to classes C_i and G_{ii} is the fraction of mass density of class C_i that is not transfered to other classes. Transfer function G is transformed in a transfer matrix G_{ij}. If we assume that agglomerates do not fuse together to generate larger agglomerates, transfer matrix G_{ij} is upper triangular; transfer of mass density from the class C_i to the class C_j with $j > i$ is equal to zero. The transfer matrix G_{ij} is given by a linear combination of the transfer matrix for erosion, $G_{ij}^{erosion}$, with the transfer matrix for rupture, $G_{ij}^{rupture}$. The typical shape of the transfer matrix $G_{ij}^{erosion}$ for Δt seconds is the following :

$$G_{ij}^{erosion} = \begin{pmatrix} 1 & \alpha+\beta & \beta & \dots & \beta \\ 0 & 1-\alpha-\beta & \alpha & 0 & 0 \\ \vdots & 0 & 1-\alpha-\beta & \ddots & \vdots \\ \vdots & \vdots & 0 & \ddots & \vdots \\ \vdots & \vdots & \vdots & \ddots & \alpha \\ 0 & \dots & \dots & \dots & 1-\alpha-\beta \end{pmatrix} \tag{3.8}$$

where α and β are the transfer rates of mass density from the class C_i to the class C_{i-1} and C_1 respectively. Those rates are obtained by calculating the area of the transfer function $G_{erosion}$, associated at class C_i, for the classes C_1 and C_{i-1} as illustrated in Figure 3.6a for the transfer function associated with the class C_4 of a mass density distribution composed of only four classes. To build the matrix 3.8, we assume that transfer fonctions $G_{erosion}$ for every classes C_i are identical. In more complex cases, values of α and β depend on the class C_i. The sum of α and β is equal to 1 only if all agglomerates of class C_i are eroded in agglomerates of the class C_{i-1} in Δt seconds, otherwise this sum is lower than 1. Typical evolution of a mass density distribution composed of 10 classes with such a transfer matrix is shown in Figure 3.7. We observe that the mass density of the class C_1 progressively increases due to erosion of the agglomerates of the class C_{10}. Erosion of those agglomerates also implies a slow transfer of mass density from the class C_{10} to the classes $C_9, C_8, \dots$

Typical shape of transfer matrix for rupture mechanism $G_{ij}^{rupture}$ for Δt seconds is the

following :

$$G_{ij}^{rupture} = \begin{pmatrix} 1 & \gamma+\lambda & \lambda & 0 & \dots & 0 \\ 0 & 1-\gamma-\lambda & \gamma & \lambda & & \vdots \\ \vdots & 0 & 1-\gamma-\lambda & \gamma & & \lambda \\ \vdots & \vdots & 0 & \ddots & & \gamma \\ \vdots & \vdots & \vdots & \ddots & & \vdots \\ 0 & \dots & \dots & \dots & & 1-\gamma-\lambda \end{pmatrix} \tag{3.9}$$

where λ and γ are rates of mass density from class C_i to classes C_j and C_{j-1} respectively. Those rates are obtained by calculating the area of the transfer function $G_{rupture}$, associated at class C_i, for classes C_j and C_{j-1} as illustrated in Figure 3.6b for the transfer function associated at the class C_4 of a mass density distribution composed of four classes. As for erosion matrix, we assume that the transfer functions $G_{rupture}$ are the same for every classes C_i. We therefore obtain the same values for γ and λ for all classes C_i. In a more complex case, values of γ and λ will depend on class C_i. The sum of γ and λ is equal to 1 only if all agglomerates of class C_i are broken up into smaller agglomerates in Δt seconds, otherwise this sum is lower than 1. Typical evolution of a given mass density distribution with such a transfer matrix is shown in Figure 3.7. We can observe a fast transfer of mass density from the class C_{10} to the classes C_5 and C_6, but no mass density is transfered at the class C_1 during the first Δt seconds. If we compare both evolutions, it clearly appears that the transfer of mass density to the different classes is faster with the rupture mechanism than with the erosion mechanism.

Such a model will strongly depend on the number of classes defined. With the choice of parent transfer function illustrated in Figure 3.6, we observe a mass density transfer even if the time step is very small. After, two increments of time, mass density of the class C_{i-2} is different of zero. We thus overestimates the decrease of the size of the agglomerates. If we now consider parent transfer function defined on the interval $[0, r_i]$ for a class C_i as illustrated in Figure 3.8, we observe a rate of transfer α equal to zero if we use coarse discretization of mass density distribution. Even if the technique to obtain the G_{ij} entries seems more relevant than in the previous case, we will never observe transfer of mass density for the class C_i to the class C_{i-1} for any time. Value of α is equal to zero at each time increment while β is different of zero. In other words, we only observe a reduction of the number of agglomerates, but never the reduction of the size of those agglomerates. Obviously, we can increase the number of classes in order to observe a transfer of mass density from the class C_i to the class C_{i-1} as illustrated in Figure 3.8b.

One of the major drawback and also one of the major advantage of this model is the large flexibility allowed in the design of parent transfer functions and the definition of corresponding coefficients G_{ij}. If we increase the number of classes, we have a model with a very large number of parameters and it will be quite difficult to have

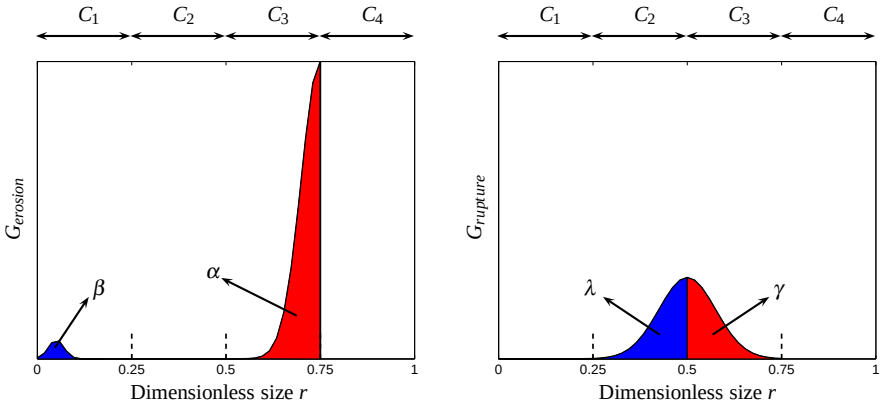

Figure 3.6: The rate of transfer α, β, λ and γ calculated to determine the transfer matrix for (a) the erosion and (b) the rupture.

experimental data to identify these parameters. However, a more elegant and simple way to model erosion is to incorporate experimental kinetic law in the mathematical model. This is the subject of the next section where we determine several continuous dispersive analytical models from the kinetic laws available in the literature.

3.3 A continuous dispersive analytical model

If we assume that all agglomerates of a given size s are dispersed in agglomerates of size r in Δt seconds with $s > r$, the evolution of mass density distribution reads :

$$\rho(r,t+\Delta t) \;=\; \rho(s,t)\,\frac{r^3}{s^3} \tag{3.10}$$

where the ratio $\frac{r^3}{s^3}$ models the loss of mass density due to dispersion of agglomerates of size s in agglomerates of size r. This loss of mass density corresponds to the mass density of tiny fragments generated during dispersion of agglomerates of size s. This mass density is given by the following expression :

$$\rho(s,t)\,\frac{s^3-r^3}{s^3} \tag{3.11}$$

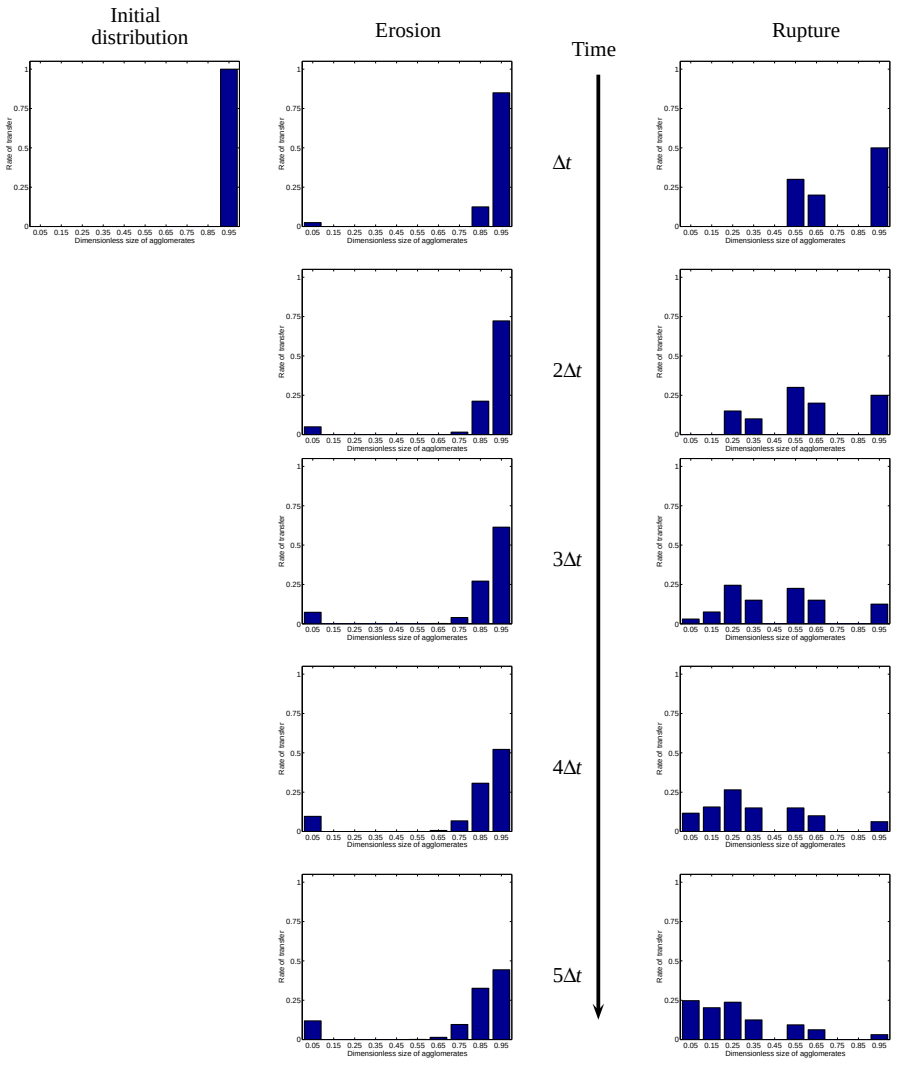

Figure 3.7: The effect of the transfer matrix $G_{erosion}$ and $G_{rupture}$ on a given mass density distribution.

If we consider that agglomerates are spherical, the equation 3.10 is easily determined by mass conservation and by conservation of the number of agglomerates. The number

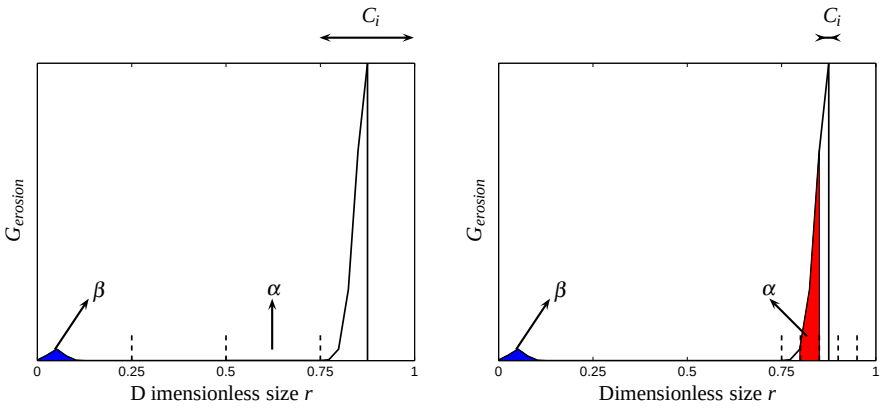

Figure 3.8: The rate of transfer α for a given time increment Δt when the number of classes is equal to (a) 4 and (b) 20.

of agglomerates of a given size s at time t is given by :

$$n(s,t) = \rho(s,t)\frac{3}{4\pi s^3 \rho_{CB}}$$

where ρ_{CB} is the density of carbon black and $n(s,t)$ is the number of agglomerates of size s. If we assume that $\rho_{CB} = 1$, we can write the following expression :

$$\begin{aligned} n(s,t) &= \rho(s,t)\frac{3}{4\pi s^3} \\ n(r,t+\Delta t) &= \rho(r,t+\Delta t)\frac{3}{4\pi r^3} \\ n(r,t+\Delta t) &= n(s,t) \end{aligned}$$

where $n(r,t)$ is the number of agglomerates of size r at time t. The equation 3.10 is determined by combining these different relations.

From the data available in the literature, we can determine which agglomerates size, s, generate agglomerates of size r in Δt seconds. For example, experimental data provides the size evolution of the agglomerates in time for a given condition. Typically, we observe :

$$\frac{4}{3}\pi r^3(t) - \frac{4}{3}\pi r^3(t+\Delta t) = K\,\Delta t \tag{3.12}$$

where is a function that depends on the initial size of the agglomerates and on the interaction between the flow and the agglomerates. This interaction can be expressed as a function of shear rate or shear stress. The relationship 3.12 can be now written as a following ordinary differential equation :

$$\frac{dr}{dt} = \frac{-K}{4\pi r^2} \tag{3.13}$$

If we assume that K is independent of r and if we define $\kappa = \frac{K}{4\pi}$, we obtain the next equation that is identical to the law proposed by Kao and Mason and by Collin and Peuvrel-Disdier :

$$\frac{dr}{dt} = \frac{-\kappa}{r^2} \tag{3.14}$$

where κ only depends on shear rate and shear stress. The size of large agglomerates decrease more slightly than the size of small agglomerates as in the peeling of potatoes. Bigger the potatoes, larger the time to peel it because the same fraction of potatoes is peeled for each Δt seconds. In the law of Collin and Peuvrel-Disdier, the variation of agglomerate volume is observed if shear stress exceeds a given value denoted called shear stress. This kinetic law is denoted as *point wise law*.

If we now assume that κ is proportional to the surface of agglomerates, given here by the product $4\pi r^2$ ($\kappa = \kappa_1 r^2$), we obtain the law proposed by Powell and Mason. Equation 3.14 then becomes :

$$\frac{dr}{dt} = -\kappa_1$$

where κ_1 depends on shear rate and shear stress. With this law, the size of all agglomerates decreases at the same velocity. Such a mechanism of dispersion is observed if the thickness of the fine layer removed along the whole surface of agglomerates at each Δt is independent of agglomerate size. This second law is denoted as *surface law*. If we suppose that κ depends on the volume of agglomerates given by the product $\frac{4}{3}\pi r^3$ ($\kappa = \kappa_2 r^3$), we find the differential equation associated at the law of Rwei et al. :

$$\frac{dr}{dt} = -\kappa_2\, r$$

This law is denoted as *volume law*. In this case, the size of agglomerates decreases faster for big agglomerates than for small agglomerates. At each time step, the size of all agglomerates decreases in the same ratio. When an agglomerate of size 1 is dispersed in an agglomerate of size 0.5 in Δt seconds, agglomerates of size 0.5 are dispersed in agglomerates of size 0.25. Finally, we can assume that parameter κ depends on the kinetic energy of agglomerates. As agglomerate has mainly a rotating motion on itself in the flow, its kinetic energy is given by the product $M\,\omega^2\,r^2$ where ω is its angular velocity and M is the agglomerate mass that is proportional to its volume. κ is then equal to $\kappa_3 r^5$. A fourth differential equation is then obtained :

$$\frac{dr}{dt} = -\kappa_3\, r^3$$

where κ_3 depends on shear rate and shear stress and also on the rotational velocity of agglomerates. This last law is denoted as *energetical law*. Units of the parameters κ, κ_1, κ_2 and κ_3 are $1/s$ if we work with a dimensionless size of agglomerates. All of those laws are valid if the agglomerate size is larger than critical size denoted r_c. Otherwise carbon black volume removed from agglomerates tends to zero and becomes

smaller than the volume of smallest entities that composed carbon black agglomerates. Here, we have to emphasize that a large number of other kinetic behaviors can be defined (Scuratti et al,2002) (Bohin et al,1996).

Let us now use the kinetics law of Kao and Mason (or the law of Collin and Disdier) to predict the size s of agglomerates that generate agglomerates of size r in Δt seconds. In such a law, κ is independent of size r and only depends on shear stress and shear rate. The size s is then given by the following relation :

$$s = \sqrt[3]{r^3 + \kappa\Delta t}$$

If we introduce this expression in equation 3.10, the evolution of the mass density distribution reads :

$$\rho(r,t+\Delta t) = \rho(\sqrt[3]{r^3 + \kappa\Delta t},t)\,\frac{r^3}{r^3 + \kappa\Delta t} \tag{3.15}$$

This equation, that only depends on the parameter κ of the kinetic law, provides the mass density evolution of any size of agglomerates r larger than critical size r_c. By replacing s by its expression in the equation 3.11, we calculate the mass density of fragments removed from agglomerates surface of size s at each Δt :

$$\rho(\sqrt[3]{r^3 + \kappa\Delta t},t)\,(\frac{\kappa\Delta t}{r^3 + \kappa\Delta t})$$

The advantage of such an approach is that the value of the parameter κ is easily extracted from experimental results.

The expression 3.15 can be seen as the solution of a specific partial differential equation by observing :

$$\begin{aligned} \rho(r,t+\Delta t)-\rho(r,t) &= \rho(\sqrt[3]{r^3+\kappa\Delta t},t)\,\frac{r^3}{r^3+\kappa\Delta t}-\rho(r,t) \\ \lim_{\Delta t\to 0}\frac{\rho(r,t+\Delta t)-\rho(r,t)}{\Delta t} &= \lim_{\Delta t\to 0}\frac{\rho(\sqrt[3]{r^3+\kappa\Delta t},t)\,\frac{r^3}{r^3+\kappa\Delta t}-\rho(r,t)}{\Delta t} \end{aligned} \tag{3.16}$$

Let us substitute the term $\rho(\sqrt[3]{r^3+\kappa\Delta t},t)\frac{r^3}{r^3+\kappa\Delta t}$ by its Taylor development :

$$\begin{aligned} \rho(\sqrt[3]{r^3+\kappa\Delta t},t)\frac{r^3}{r^3+\kappa\Delta t} &= \rho(r,t) + \\ &\Delta t\left\{\frac{\partial\rho(r,t)}{\partial r}\frac{1}{3}\frac{\kappa}{\sqrt[3]{(r^3+\kappa\Delta t)^2}}\frac{r^3}{r^3+\kappa\Delta t}+\rho(\sqrt[3]{r^3+\kappa\Delta t},t)\frac{-\kappa r^3}{(r^3+\kappa\Delta t)^2}\right\}_{\Delta t=0} \\ &+\Delta t^2\cdots \end{aligned}$$

We then obtain :

$$\lim_{\Delta t \to 0} \frac{\rho(r,t+\Delta t)-\rho(r,t)}{\Delta t} =$$
$$\lim_{\Delta t \to 0} \left\{ \frac{1}{\Delta t}\rho(r,t) + \frac{\Delta t}{\Delta t}\left(\frac{\partial \rho(r,t)}{\partial r}\frac{\kappa}{3r^2} + \rho(r,t)\frac{-\kappa}{r^3}\right) + \frac{\Delta t^2}{\Delta t}\cdots - \frac{1}{\Delta t}\rho(r,t) \right\}$$

And we finally derive the partial differential model associated :

$$\frac{\partial \rho(r,t)}{\partial t} = \frac{\partial \rho(r,t)}{\partial r}\frac{\kappa}{3r^2} - \frac{\kappa \rho(r,t)}{r^3}$$

We present in Table 3.1, the differential equations obtained with the different kinetics laws presented previously. With these models, we are able to obtain in one calculation the evolution of the mass density distribution for any time step if value of κ does not change in time. A lot of calculation time is also saved because those models do not depend on complex transfer matrices. We now have a family of models that are able to predict the evolution of agglomerates size in time. But each of these models provides different evolutions of agglomerate size because they depend of different kinetic law. For a better understanding of the behavior of these models, let us now study in detail each kinetic law through a sensitivity analysis.

Kinetics laws	Analytical models	Differential models
Point wise law $\frac{dr}{dt} = -\frac{\kappa}{r^2}$ $r(t) = \sqrt[3]{r(0)^3 - \kappa t}$	$\rho(r,t) =$ $\rho(\sqrt[3]{r(0)^3 + \kappa t}, t)\frac{r(0)^3}{r(0)^3 + \kappa t}$	$\frac{\partial \rho(r,t)}{\partial t} =$ $\frac{\partial \rho(r,t)}{\partial r}\frac{\kappa}{3r^2} - \frac{\kappa \rho(r,t)}{r^3}$
Surface law $\frac{dr}{dt} = -\kappa_1$ $r(t) = r(0) - \kappa_1 t$	$\rho(r,t) =$ $\rho(r(0) + \kappa_1 t, t)\frac{r(0)^3}{(r(0) + \kappa_1 t)^3}$	$\frac{\partial \rho(r,t)}{\partial t} =$ $\frac{\partial \rho(r,t)}{\partial r}\kappa_1 - 3\kappa_1 \rho(r,t)$
Volume law $\frac{dr}{dt} = -\kappa_2 r$ $r(t) = r(0)e^{-\kappa_2 t}$	$\rho(r,t) =$ $\rho(r(0)e^{\kappa_2 t}, t)\frac{r(0)^3}{r(0)^3 e^{3\kappa_2 \Delta t}}$	$\frac{\partial \rho(r,t)}{\partial t} =$ $\frac{\partial \rho(r,t)}{\partial r}\kappa_2 r - 3\kappa_2 \rho(r,t)$
Energetical law $\frac{dr}{dt} = -\kappa_3 r^3$ $r(t) = \frac{r(0)}{\sqrt{(2\kappa_3 t r(0)^2 + 1)}}$	$\rho(r,t) =$ $\rho(\frac{r(0)}{\sqrt{1 - 2\kappa_3 r(0)^2}}, t)\sqrt{(1 - 2\kappa_3 t r(0)^2)^3}$	$\frac{\partial \rho(r,t)}{\partial t} =$ $\frac{\partial \rho(r,t)}{\partial r}\kappa_3 r^3 - 3\kappa_3 r^2 \rho(r,t)$

Table 3.1: Kinetic laws and the analytical and partial differential models associated.

3.4 Sensitivity analysis of the kinetics law

From the observation of the shape of the differential equation associated at each kinetics law, it clearly appears that the evolution of the agglomerates size r depends on the law selected. It is impossible to obtain the same evolution of r in giving the same value at the parameters κ, κ_1, κ_2 and κ_3. Nevertheless, it is possible to determine a set of values for κ, κ_1, κ_2 and κ_3 that minimize the deviation, in the least-square sense, between the different evolutions of r obtained with these laws during a given time. Without lost of generality, we here consider that these parameters are constant in time as in simple shear flow.

To determine these set of parameters, we firstly calculate a reference evolution of r by using the point wise law with $\kappa = 2.5\,10^{-5}$. The pointwise law is selected as reference law because it seems the more appropriate law to predict the evolution of single agglomerate in rubber in our case (Collin,2004). The value of κ is the value determined by Cemef group during their experiments. The initial value of r ($t = 0$) is choosen (arbitrary) as equal to 0.8. The value of κ_1, κ_2 and κ_3 are then optimized to minimize the deviation between this reference evolution and the evolutions of r obtained with the surface, volume and energetical laws respectively. As illustrated in Figure 3.9, similar evolutions of r are obtained during 20000 seconds with the set of parameters (κ, κ_1, κ_2 and κ_3) given in Table 3.2. But deviation between the evolutions of r increases when the time reaches and exceeds 20000 seconds. Ratio $\frac{dr}{dt}$ increases with volume and energetical laws to tend to zero and decreases with point wise law to tend to $-\infty$. With surface law, this ratio is constant.

If we use this set of parameters to obtain the evolution of r from $r = 1$, we observe that the time needed to reach $r = 0.8$ depends on the kinetic laws as illustrated in Figure 3.10. From $r = 0.8$, we obtain the same evolution of r than in previous example but shifted in time. The four sections of curves represented in red corresponds to the

Initial size r	The parameters of the kinetic law (s^{-1})			
	κ	κ_1	κ_2	κ_3
$r = 0.8$	$2.5\,10^{-5}$	$2.02\,10^{-5}$	$3.05\,10^{-5}$	$6.9\,10^{-5}$

Table 3.2: Values of κ, κ_1, κ_2 and κ_3 when r is equal to 0.8

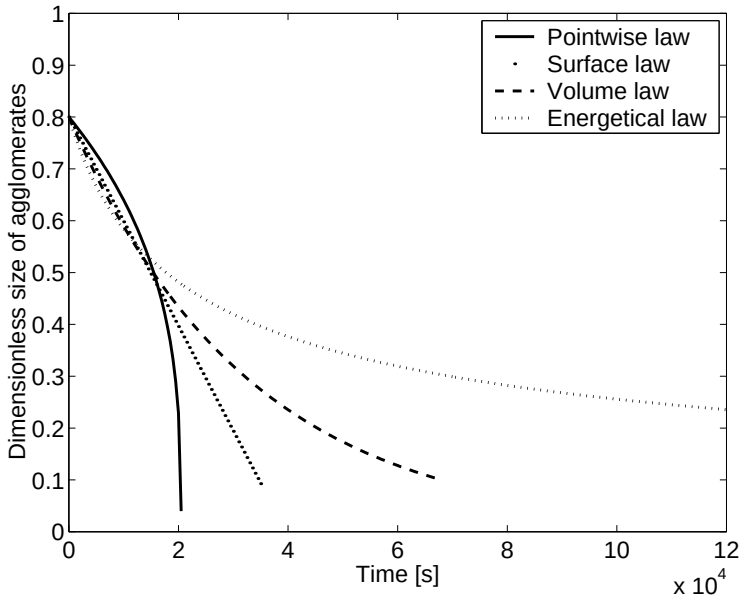

Figure 3.9: Evolution of the agglomerates size in time as a function of the kinetic law when the size r is initially equal to 0.8.

evolution of $r(t)$ observed in Figure 3.9 from $t = 0$ to $t = 20000$. Deviation between those red curves is therefore minimum with the set of parameters selected.

In order to evaluate the effect of the kinetic laws on the evolution of a given mass density distribution, we calculate the evolution in time of a gaussian distribution centered at $r = 0.8$ with the different models. These simulations are performed with the same set of values for the parameters (κ, κ_1, κ_2 and κ_3) than previously (Table 3.2). The critical size r_c under which we do not predict the evolution of this mass density distribution is imposed at 0.05. It clearly appears that the maximum of mass density moves along r as predicted in Figure 3.9. For time lower than 15000 seconds, it moves faster with energetical model than with pointwise model, but this trend changes when time reaches 15000 seconds. In the same time, the width of mass density distribution decreases with energetical and volume models and increases with pointwise model. With surface model, width is almost constant. However, the mass density of small fragments generated during the agglomerates dispersion depends on the model as illustrated in Table 3.3. This mass density increases faster with energetical model than with pointwise model. Intermediate mass density of small fragments is obtained with surface and volume models. Distributions of agglomerates obtained with energetical,

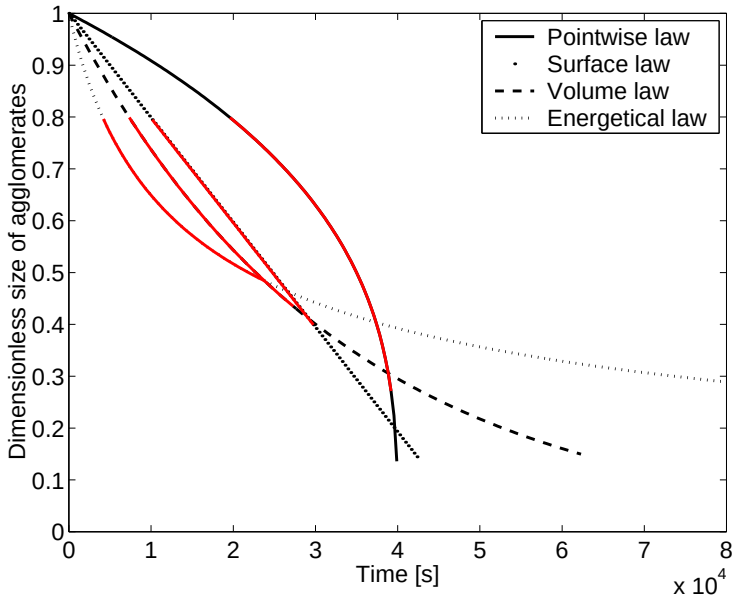

Figure 3.10: Evolution of the agglomerates size in time as a function of kinetic laws when the size r is initialy equal to 1.

volume and surface models are composed of a small number of agglomerates with a dimensionless size around 0.477, 0.439 and 0.410 and a large number of small fragments with a dimensionless size smaller than 0.05. These parts of the distributions are not represented in the Figure 3.11. With pointwise model, we have a wider distribution of agglomerates of various sizes between 0.2 and 0.7 and a smaller amount of mass eroded. Dynamics of the mass density distribution clearly depends on the model chosen even if we select a set of parameters (κ, κ_1, κ_2 and κ_3) that provide a similar evolution of r during a given time. Let us now compare the quality of each model to predict the evolution of a given mass density distribution of carbon black in simple shear flow. The experimental evolutions of the mass density distribution, considered as reference evolutions, are measured with the *dispergrader*.

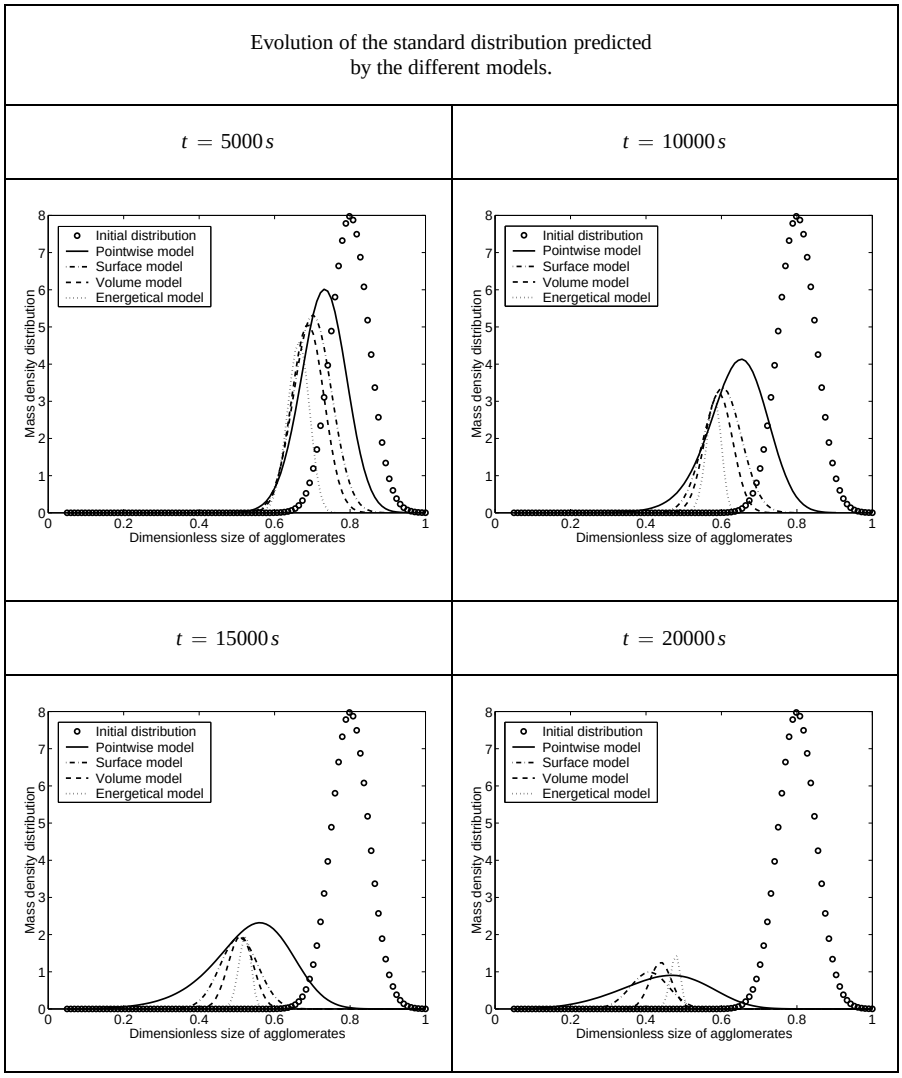

Figure 3.11: Evolution of a given mass density distribution in time with the different models.

Model	Times (s)			
	5000	10000	15000	20000
Pointwise model	0.09	0.21	0.41	0.73
Surface model	0.33	0.58	0.76	0.88
Volume model	0.45	0.70	0.84	0.91
Energetical model	0.66	0.85	0.92	0.95

Table 3.3: Evolution of the mass density of small fragments ($r < 0.05$) vs. the time for each model.

3.5 The *dispergrader* data

Quality of continuous dispersive analytical models is evaluated by predicting the evolution of an experimental mass density distribution in a given flow. Experimental evolution of this mass density distribution is obtained in mixing styrene-co-butadiene rubber and carbon black agglomerates in a Mooney rheomether. The rotor of the Mooney rheomether used in these experiments is conical and its rotation generates a simple shear flow. The shear rate observed in this flow depends on the velocity of the rotor. Three different cases are considered : $2\,rpm$, $5\,rpm$ and $10\,rpm$ that corresponds to a shear rate of $1\,s^{-1}$, $2.5\,s^{-1}$ and $5\,s^{-1}$ respectively. The sample of rubber introduced in the Mooney chamber already contains carbon black agglomerates. These agglomerates are relatively well distributed in the whole rubber sample but their dispersion is not perfect. The Mooney rheometer allows us to improve this dispersion. With the *dispergrader*, we measure the evolution of the dispersion of carbon black agglomerates in rubber as explained in chapter 1. The state of dispersion is characterized by a first histogram that represents the cumulative surface s_i associated at each class of size of agglomerates C_i and by a second histogram that provides the number of surface in each class. By sake of simplicity, let us assume that $\sum_{i=1}^{K} s_i = 1$ at the start of the mixing with K the total number of class.

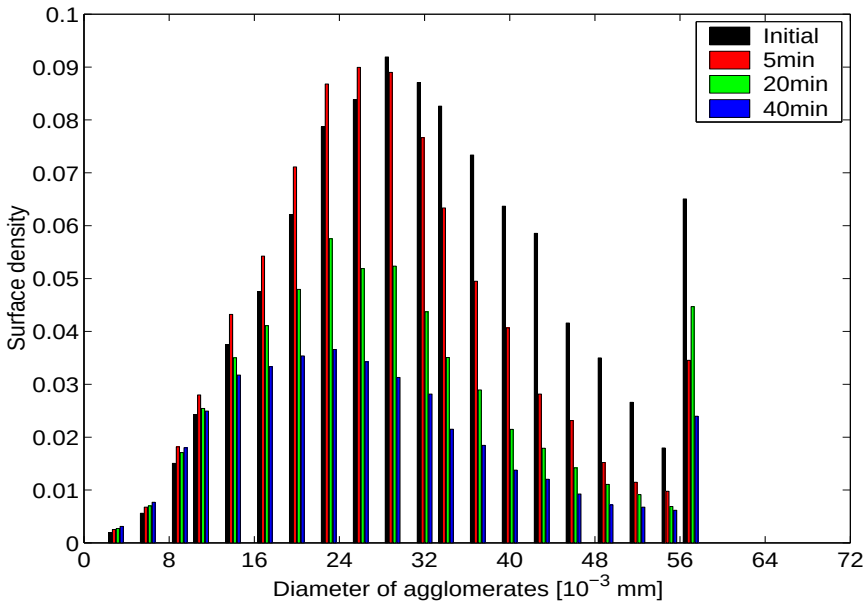

(a)

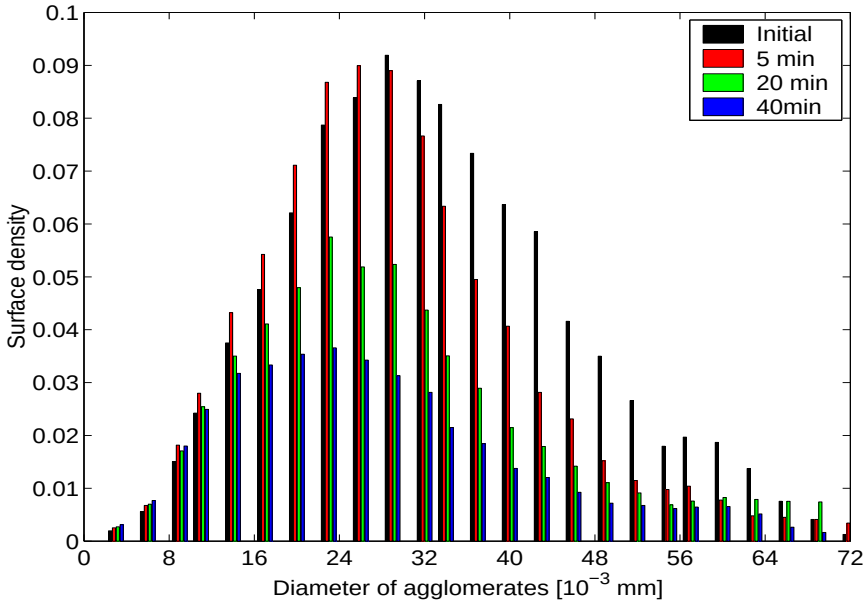

(b)

Figure 3.12: (a) The surface density histograms built from the data of the dispergrader for the experiment performed at $2rpm$ and (b) the surface density histogram obtained when we distribute the surface density of the class $57\mu m$ on the interval $[57\mu m, 72\mu m]$.

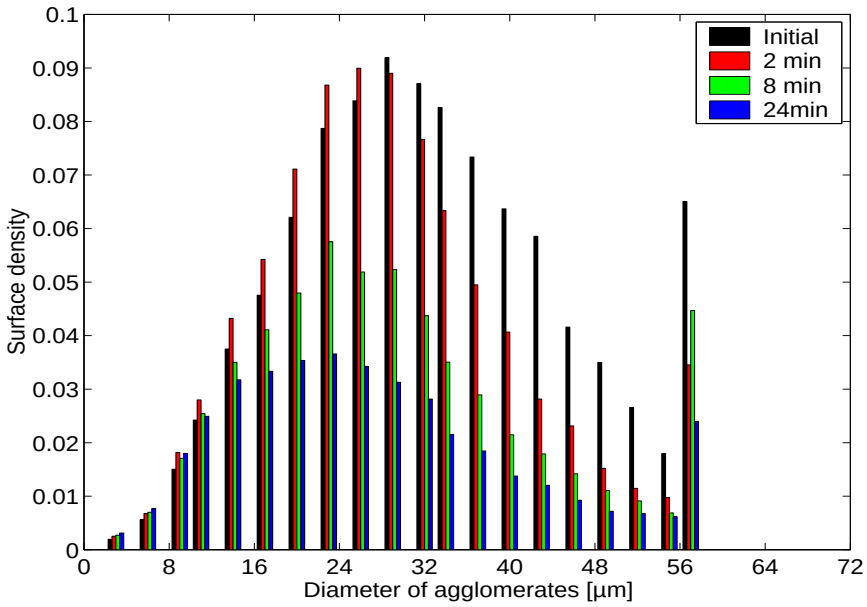

(a)

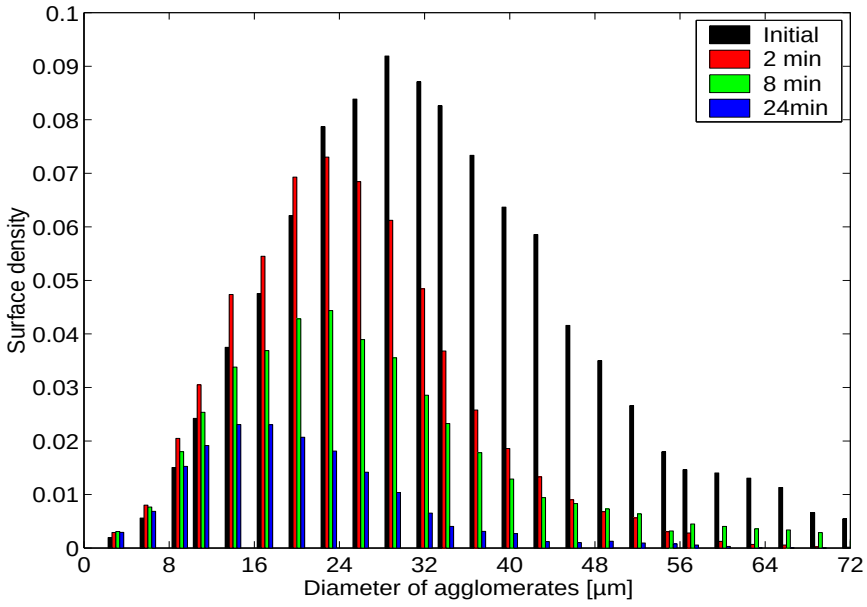

(b)

Figure 3.13: (a) The surface density histograms built from the data of the Dispergrader for the experiment performed at $5rpm$ and (b) the surface density histograms obtained when we distribute the surface density of the class $57\mu m$ on the interval $[57\mu m, 72\mu m]$.

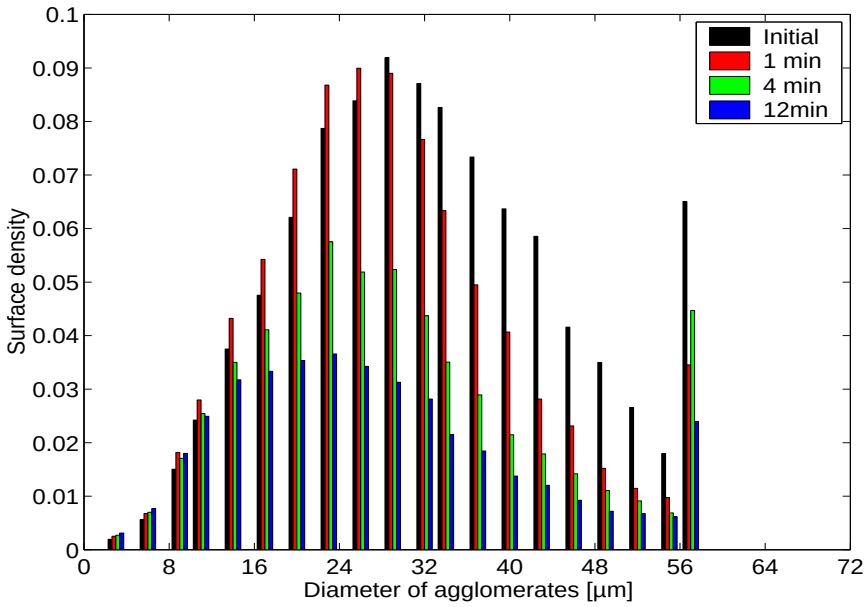

(a)

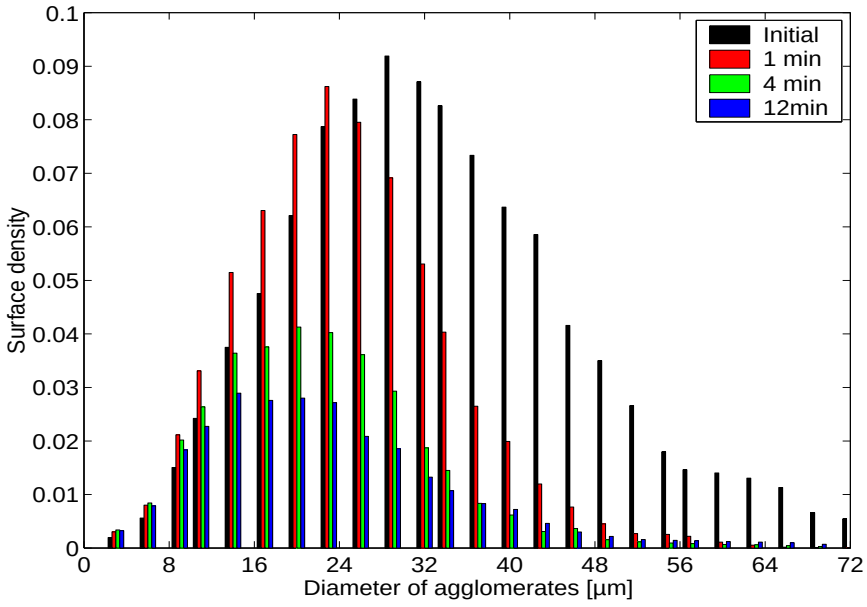

(b)

Figure 3.14: (a) The surface density histograms built from the data of the Dispergrader for the experiment performed at $10rpm$ and (b) the surface density histograms obtained when we distribute the surface density of the class $57\mu m$ on the interval $[57\mu m, 72\mu m]$.

As illustrated in Figure 3.12a for the experiment at $2\,rpm$, we observe that the $\sum_{i=1}^{K} s_i$ decreases progressively during the mixing because the *dipergrader* is not able to detect the tiny fragments, with a size smaller than $3\mu m$, generated by the dispersion of the big agglomerates (larger than $3\mu m$). This effect is also observed in the experiments at $5\,rpm$ and $10\,rpm$. As explained previously, the dispergrader ranks in the largest class $57\mu m$ all the surfaces with a typical size larger than $57\,\mu m$ and this explains the peak observed in the Figure 3.12a, 3.13a, 3.14a, in the class $57\,\mu m$. This peak indicates that it exists in the mix a given amount of agglomerates larger than $57\,\mu m$. We decide to distribute this amount of surface density on several classes between $57\,\mu m$ and $72\,\mu m$ to eliminate this "anomaly".

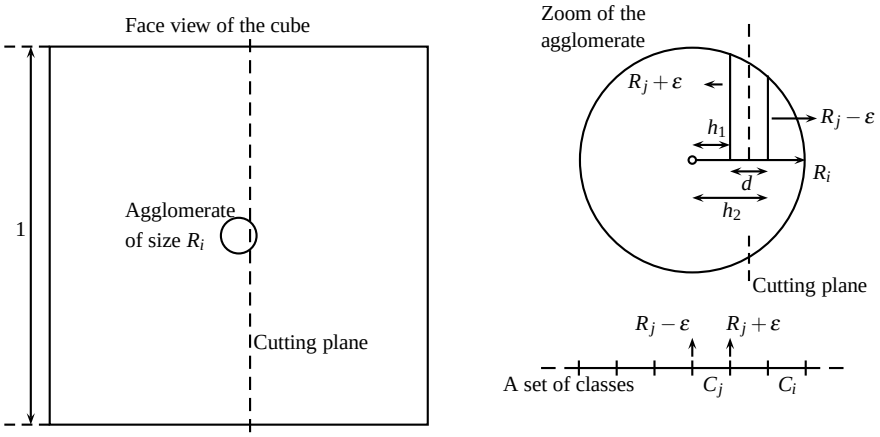

Figure 3.15: The probability to cut the agglomerate and to obtain a circle with a radius between $R_j+\varepsilon$ and $R_j-\varepsilon$ is equal to the distance $2d$.

The continuous dispersive analytical models predict the evolution of a mass density distribution in time and not directly the evolution of a surface density distribution. Therefore, it is necessary to transform a surface density distribution s in the equivalent mass density distribution ρ. Let us consider a uniform distribution of spherical agglomerates in a cube of large size in comparison with the agglomerates size. In other words, we assume that the sizes of the agglomerates, R_i, are small in comparison of a unitary box ($R_i << 1$). From this distribution, we calculate a mass density distribution composed of K classes characterized by a typical size R_i and such that $R_{i+1} - R_i = \varepsilon$.

The mass density of agglomerates ρ_i of the class C_i is given by the following relation :

$$\rho_i = n_i \frac{4\pi R_i^3}{3}$$

where n_i is the number of agglomerates contained in the class C_i. By analogy to the protocol used to obtain the experimental surface density histogram, we cut this cube by a plane parallel to one of its face. The probability P_{ij} that the intersection between an agglomerate of size R_i and this plane be a surface that could be ranked in the class C_j corresponds to the distance $2d$. The distance d is illustrated in Figure 3.15 and depends on the couple (R_i,R_j) considered. The probability P_{ij} for each couple (R_i,R_j) is given by the following relation :

$$\begin{cases} P_{ij} = 2(\underbrace{\sqrt{R_i^2-(R_j-\varepsilon)^2}}_{h_2} - \underbrace{\sqrt{R_i^2-(R_j+\varepsilon)^2}}_{h_1}) & if\ R_i > R_i \\ P_{ij} = 2\sqrt{2R_i\varepsilon-\varepsilon^2} & if\ R_j = R_i \\ P_{ij} = 0 & if\ R_j > R_i \end{cases}$$

From this expression, we build a matrix of probability that is upper triangular. With this matrix, we estimate the number of surface ranked in each class N_j, when we cut the cube by a given plane, as a function of the number of agglomerates n_i contained in the cube :

$$N_j = \sum_{i=1}^{K} P_{ij} n_i$$

This relation is only valid if the distribution of the agglomerates in the cube is uniform and if the number of agglomerates contained in each class is high. If we assume that all the surfaces ranked in the class C_j have a surface equal to $4\pi R_j^2$, the surface density

is given by the following relation :

$$\begin{aligned} s_j &= 4\pi R_j^2 N_j \\ &= 4\pi R_j^2 \sum_{i=1}^{K} P_{ij} n_i \\ &= 4\pi R_j^2 \sum_{i=1}^{K} \frac{3P_{ij}}{4\pi R_i^3} \rho_i \\ &= R_j^2 \sum_{i=1}^{K} \frac{3P_{ij}}{R_i^3} \rho_i \\ &= 3R_j^2 \sum_{i=1}^{K} \frac{P_{ij}}{R_i^3} \rho_i \end{aligned}$$

The relation between s_i and ρ_j reads :

$$s_i = A_{ij}\, \rho_j$$

Finally, we transform a surface density distribution in an equivalent mass density distribution, by writting :

$$\rho_i = A_{ij}^{-1}\, s_j$$

It is important to keep in mind that the mass density distribution obtained by this calculation is not the real mass density distribution but only an approximation of this distribution. We now use this technique to calculate the mass density distribution associated at each surface density distribution obtained with the *dispergrader*. As for the surface density distribution, the sum of all the values ρ_i ($i = 1..K$) is only equal to 1 at the start of the mixing. The evolution of the surface density distributions and the equivalent evolution of mass density histograms obtained at $2\,rpm$, $5\,rpm$ and $10\,rpm$ are illustrated in Figure 3.16, 3.17 and 3.18 respectively. We observe on those figures that the mass density distributions are not as smooth as the surface density distributions. The small oscillations of the mass density come from the transformation of the surface density distribution in a mass density distribution. We therefore decide to fit those distributions by a six-order polynome to obtain a smooth evolution of the mass density. This data are now used to evaluate the quality of each model to predict the evolution of experimental mass density distributions in simple shear flow.

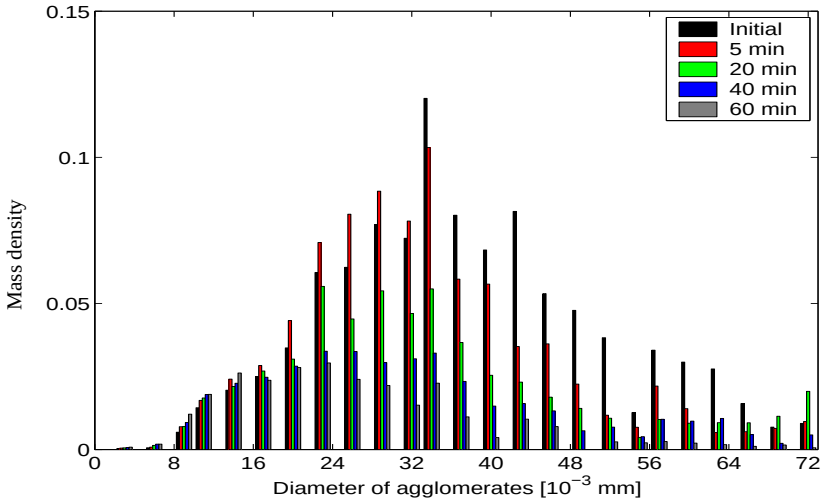

(a)

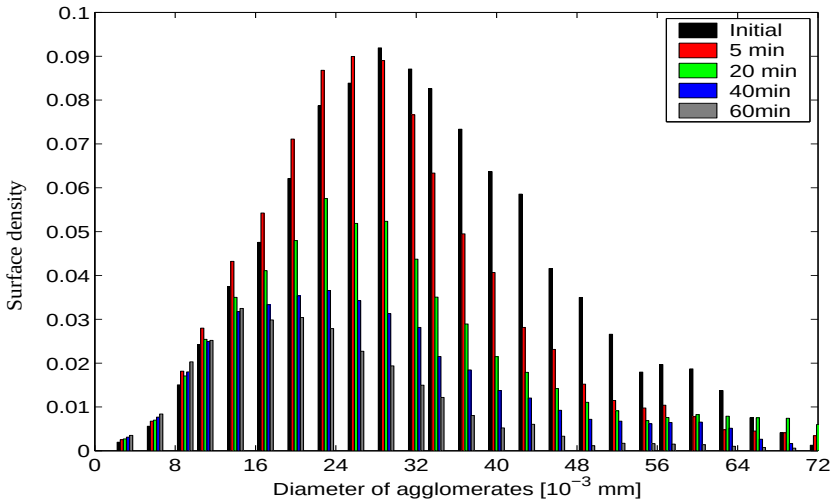

(b)

Figure 3.16: (a) The mass density distributions built with the probability matrix from the surface density distributions for the experiment performed at $2\,rpm$ in the Mooney rheometer and (b) the surface density distributions associated.

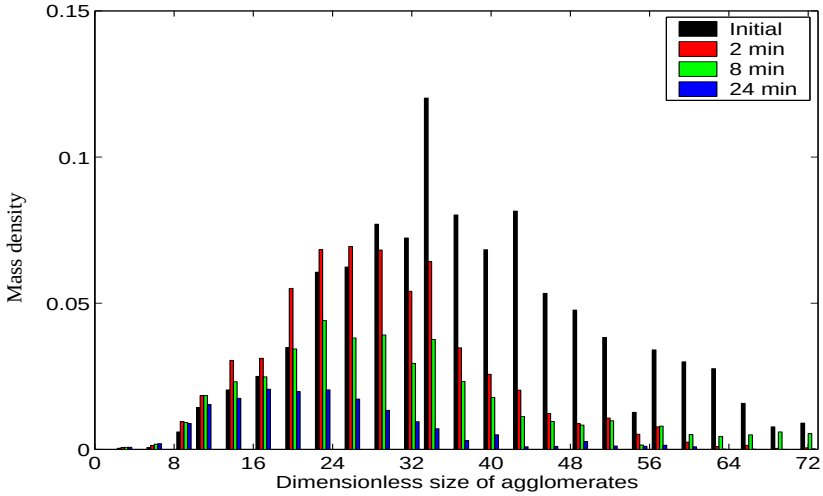

(a)

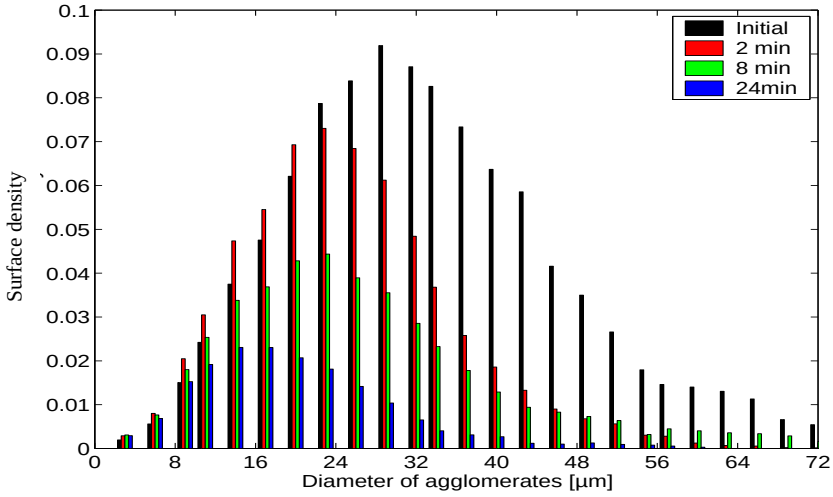

(b)

Figure 3.17: (a) The mass density distributions built with the probability matrix from the surface density distributions for the experiment performed at $5\,rpm$ in the Mooney rheometer and (b) the surface density distributions associated.

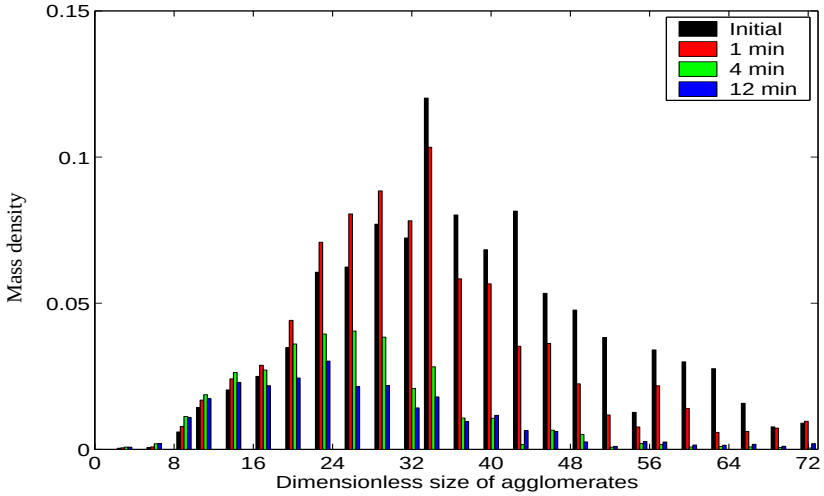

(a)

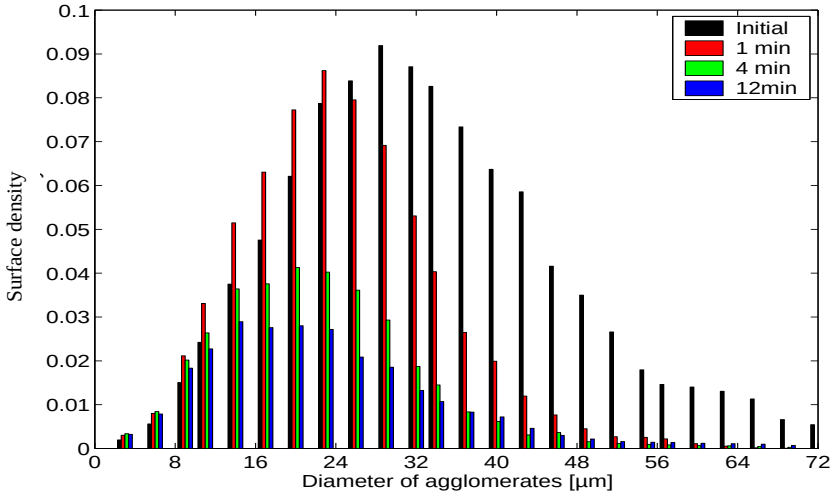

(b)

Figure 3.18: (a) The mass density distributions built with the probability matrix from the surface density distributions for the experiment performed at $10\,rpm$ in the Mooney rheometer and (b) the surface density distributions associated.

3.6 Comparison of the experimental data with numerical results

To investigate the quality of our continuous dispersive analytical models, we consider the mass density distribution of the agglomerates measured with the *dispergrader* in the Mooney experiments. We then calculate the evolution of this mass density distribution in time with the different models. This evolution is compared to the evolution of this mass density distribution in the Mooney rheometer. This evolution is obtained in measuring at different time of mixing the state of dispersion of the agglomerates in the rubber with the *dispergrader*. In such an approach, we assume that the mix rubber-carbon black is homogeneous during the mixing and we consider that the shear rate is the same in the whole Mooney chamber. The evolution of the experimental mass density distribution is therefore independent of the area where the measure is performed during the experiment.

The domain of comparison between numerical and experimental results is limited to the interval $[16\,\mu m, 56\,\mu m]$ because the quality of the measure performed by the *dispergrader* outside this interval is low. In the interval $[3\,\mu m, 16\,\mu m]$, the *dispergrader* does not detect a modification of the mass density distribution during all the mixing as if the dispersion does not occur for such size of agglomerates. This result is quite surprising and the evolution of this part of the mass density distribution is not taken into account in our analysis. Moreover, the evolution of the mass density distribution in the interval $[57\,\mu m, 72\,\mu m]$ depends on the distribution of the peak of mass density observed in $57\,\mu m$ in this interval. As we do not know the validity of this transformation, the evolution of the mass density distribution in this interval is not analyzed. Let us now consider the experimental result obtained for the evolution of the mix rubber-carbon black in the experiment at $2\,rpm$. Firstly, we determine the value for the parameters κ, κ_1, κ_2 and κ_3 that provides the best agreement between the experimental and numerical results at $2\,rpm$. Secondly, these parameters are used to predict the evolution of the mass density distribution in the experiments at $5\,rpm$ and $10\,rpm$. In these two cases, the values of κ, κ_1, κ_2 and κ_3 are not adapted to obtain the best fit between experimental and numerical results. In the case at $2\,rpm$, the simple shear flow is characterized by a constant shear rate equal to $1\,s^{-1}$ and a shear stress equal to $126000\,Pa$.

Collin and Peuvrel-Disdier propose the following formulation for the parameters κ (Collin et al,2004) :

$$\begin{cases} \kappa = \alpha\,(\sigma - \sigma_c)\dot{\gamma} & \text{if } \sigma > \sigma_c \\ \kappa = 0 & \text{if } \sigma \leq \sigma_c \end{cases}$$

where α is a constant, σ is the shear stress, σ_c is the critical shear stress and $\dot{\gamma}$ is the

Parameters	α $[\mu m^3 Pa^{-1}]$	τ_c $[Pa]$
Styrene Butadiene rubber	$1.78\ 10^{-5}$	71400

Table 3.4: The value of the parameters of the law proposed by Cemef group to calculate the value of κ. These values are relevant only for carbon black agglomerates $N234$.

shear rate. The value of those different parameters depends on the kind of rubber and on the property of carbon black. The values determined by the Cemef group for the carbon black $N234$ in styrene-co-butadiene rubber are given in Table 3.4. These values were determined to fit the experimental evolution of the size of a single agglomerates in a simple shear flow of styrene-co-butadiene rubber.

The value of the parameters κ_1, κ_2 and κ_3 is determined to obtain the same evolution with all models of the agglomerates with an inital size equal to $44\,\mu m$ during 3600 seconds. The value of κ, calculated from the data provided by Cemef group, is equal to $0.97\,\frac{\mu m^3}{s}$. The parameters κ_1, κ_2 and κ_3 are respectively equal to $7.36\,10^{-4}\,\frac{\mu m}{s}$, $3.50\,10^{-5}\,s^{-1}$ and $7.34\,10^{-8}\,\frac{1}{s\,\mu m}$. We select the size $44\mu m$ as reference size because the mass density distribution is maximum for this size of agglomerates. We thus follow the same approach than in the sensibility analysis.

As shown in Figure 3.19, we do not obtain a very good agreement between the numerical and experimental results with these values of the parameters. But, we have to keep in mind that the value of κ is determined from the results obtained by Collin and Peuvrel-Disdier for a mix that contains a very small concentration of agglomerates. In their experiments, the only mechanism observed is the erosion and the agglomerate is considered as alone in the rubber matrix. In the Mooney experiments, the rubber contains around 20% of volume fraction of carbon black and we therefore observe other mechanisms as collision that increases the efficiency of the dispersion. Moreover, it is highly difficult to evaluate the initial state of the agglomerates in the Mooney experiments unlikely to the experiments of Cemef where all the experimental conditions are well controlled. The initial state of the agglomerates depends on the level of infiltration of the matrix in the agglomerates and on the stress acting on these agglomerates by the rubber or/and by the mixer during the setting of the initial mix rubber-carbon black that we introduced in the Mooney rheometer. Nervetheless, it exists a set of parameters that improves the results provided by each model as illustrated in Figure 3.20. The best agreement between experimental and numerical results is then observed with the volume model. In this case, the parameters are equal to $2.25\,\frac{\mu m^3}{s}$, $2.3\,10^{-3}\,\frac{\mu m}{s}$,

$1.2\,10^{-4}\,s^{-1}$ and $4\,10^{-7}\,\frac{1}{s\,\mu m}$ for κ, κ_1, κ_2 and κ_3 respectively. These values are determined in minimizing the error between experimental and numerical distributions in least-square sense.

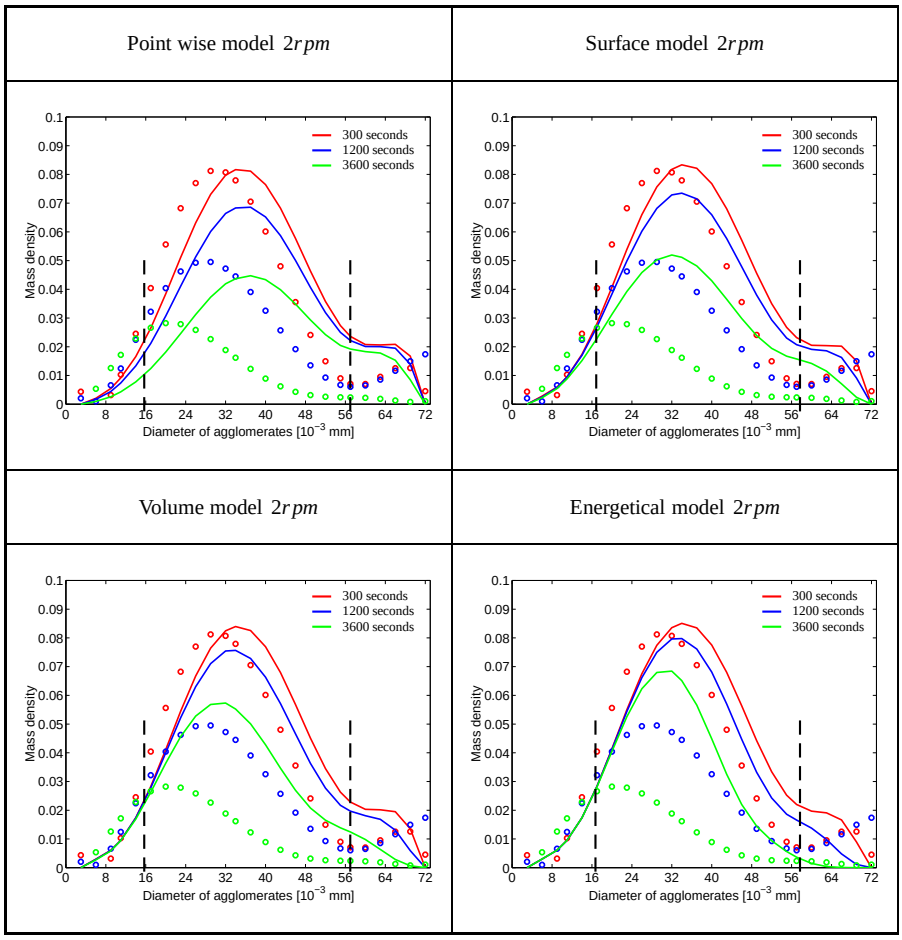

Figure 3.19: The mass density distributions predicted by the different continuous models at $2rpm$ vs. the experimental mass density distributions. The values of κ, κ_1, κ_2 and κ_3 are respectively equal to $0.97\,\frac{\mu m^3}{s}$,$7.36\,10^{-4}\,\frac{\mu m}{s}$, $3.5\,10^{-5}\,s^{-1}$ and $7.34\,10^{-8}\,\frac{1}{s\,\mu m}$.

A second set of experimental results were obtained at $10\,rpm$. In such a case, the ro-

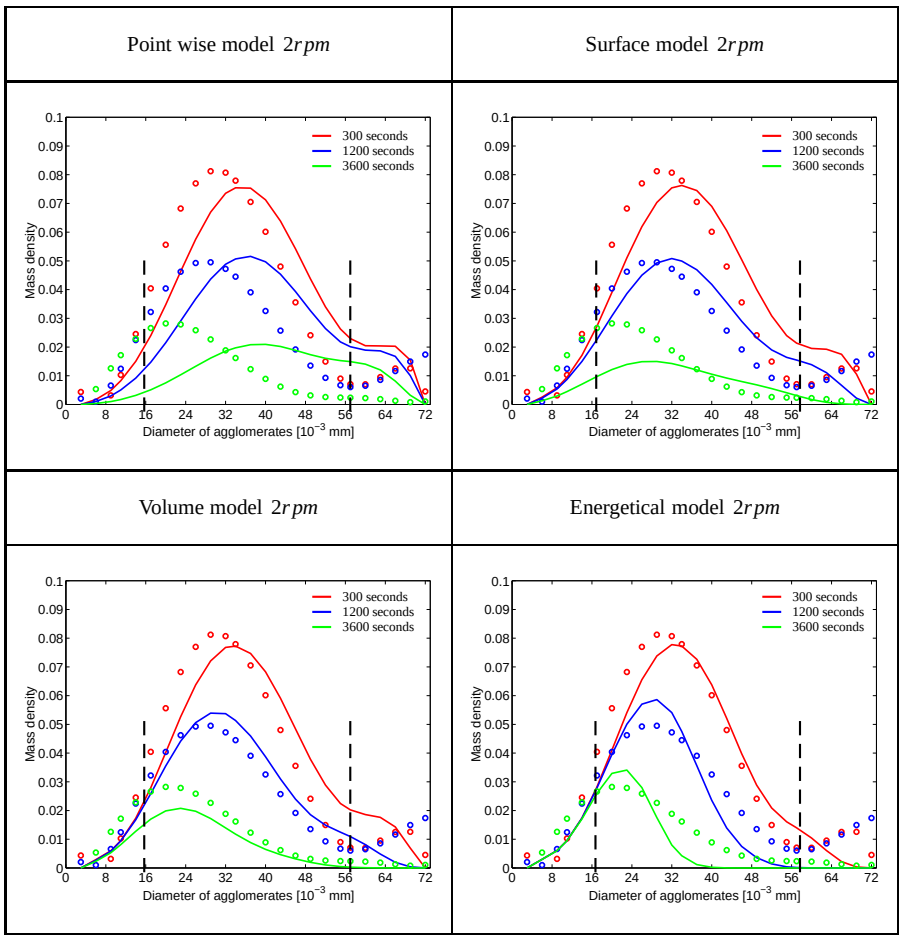

Figure 3.20: The mass density distributions predicted by the different continuous models at $2rpm$ with the second set of parameters vs. the experimental mass density distributions. The values of κ, κ_1 κ_2 and κ_3 are equal to $2.25\,\frac{\mu m^3}{s}$, $2.3\,10^{-3}\,\frac{\mu m}{s}$, $1.2\,10^{-4}s^{-1}$ and $4\,10^{-7}\,\frac{1}{s\,\mu m}$.

tating motion of the rotor in the Mooney chamber generates a simple shear flow with a shear rate of $5s^{-1}$. Those experiments are performed during a maximum of 720 seconds. The product $\dot{\gamma}t$ is kept constant between those experiments and the experiments performed at $2\,rpm$. The value of the parameters considered in this calculation

are obtained in multiplying the value of κ, κ_1, κ_2 and κ_3 used in the case at $2\,rpm$ by 5 to take into account the increase of the shear rate by a factor 5. They are not determined by minimizing the error between the experimental and numerical results. These values are given in Table 3.5. With this set of parameters, the same evolution of the mass density distribution is obtained than for the case at $2\,rpm$. A surprisingly good agreement is observed with the volume model for these data, even if some small shifts are observed for intermediate curves. Those deviations can be explained by the non-continuum character of the process including collision and rupture, but also by some of the exact time of the measurement performed during one experimental work. Finally, we show in Figure 3.22 the numerical results obtained for the experiments at $5\,rpm$. The value of κ, κ_1, κ_2 and κ_3 used in this calculation are not determined by curve fitting approach but they are obtained in multiplying the value of the parameters at $2\,rpm$ by 2.5 to take into the increase of the shear rate. The values of these parameters are given in Tables 3.5. The quality of the prediction of our models is slightly lower than in the experiments at $2\,rpm$ as for the case at $10\,rpm$. Small shifts are observed for intermediate curves. Those deviations have probably the same origins than in the experiments at $10\,rpm$.

The comparison between experimental and numerical evolutions of the mass density shows that our models predict the complex dynamics of the mass density distribution in a given flow. But, the quality of the prediction strongly depends on the model considered. A very good agreement between experimental and numerical results is reached only with one parameter for the whole set of data. Obviously, these results could be improved in adaptating the value of the parameters in time. In each experiment, the model that provides the best results is the volume model. Initially, such an observation slightly disappoints us because we thought that the pointwise model would provide the best results. The pointwise model is linked to the kinetics law determined by Collin and Disdier to predict the dispersion of the same kind of carbon black agglomerates than in this experiment and the same rubber. Moreover, the way followed by Collin and Disdier to model the erosion is close to our idea of the erosion process.

But, we have to keep in mind that the mechanism of rupture and erosion can occur simultaneously in the Mooney experiments. For example, in the experiments at $2\,rpm$, all the agglomerates larger than $66\mu m$ could break-up in several fragments. This critical size decreases with the increase of the rotor velocity to reach $46\,\mu m$ and $36\,\mu m$ for the experiments at $5\,rpm$ and $10\,rpm$ respectively. As the mass concentration of carbon black in the rubber is high, each agglomerate interacts with its neighborhood and the shear rate flow around the agglomerates is modified. A collision between two agglomerates is sometimes observed.

Those differences between the experiments performed in the Mooney rheometer and

the conditions in which the Cemef group determined their law might explain a part of the deviations observed between the prediction of the pointwise model and the experimental results. Unlikely to the pointwise law, the volume law predicts that the size of the large agglomerates decreases faster than the size of the small agglomerates. This approach of the dispersion mechanism is at the boundary between the mechanism of erosion and the mechanism of rupture. This way to model the dispersion mechanisms is therefore more appropriate to predict the evolution of the mass density distribution in the Mooney experiments.

Experiment	Parameters of model			
	$\kappa\ [\frac{\mu m^3}{s}]$	$\kappa_1\ [\frac{\mu m}{s}]$	$\kappa_2\ [s^{-1}]$	$\kappa_3\ [\frac{1}{s\,\mu m}]$
$2\,rpm$	2.25	$2.3\,10^{-3}$	$1.2\,10^{-4}$	$4\,10^{-7}$
$5\,rpm$	5.6	$0.57\,10^{-2}$	$3\,10^{-4}$	$9.9\,10^{-7}$
$10\,rpm$	11.25	$1.15\,10^{-2}$	$6\,10^{-4}$	$1.9\,10^{-6}$

Table 3.5: Values of κ, κ_1, κ_2 and κ_3 for the experiment at $2\,rpm$, $5\,rpm$ and $10\,rpm$. The value for the experiment at $2\,rpm$ have been determined to obtain the best fit between experimental and numerical results. The value for the experiments at $5\,rpm$ and $10\,rpm$ are extrapolated from the values at $2\,rpm$ in taken into account the increasing of the shear rate.

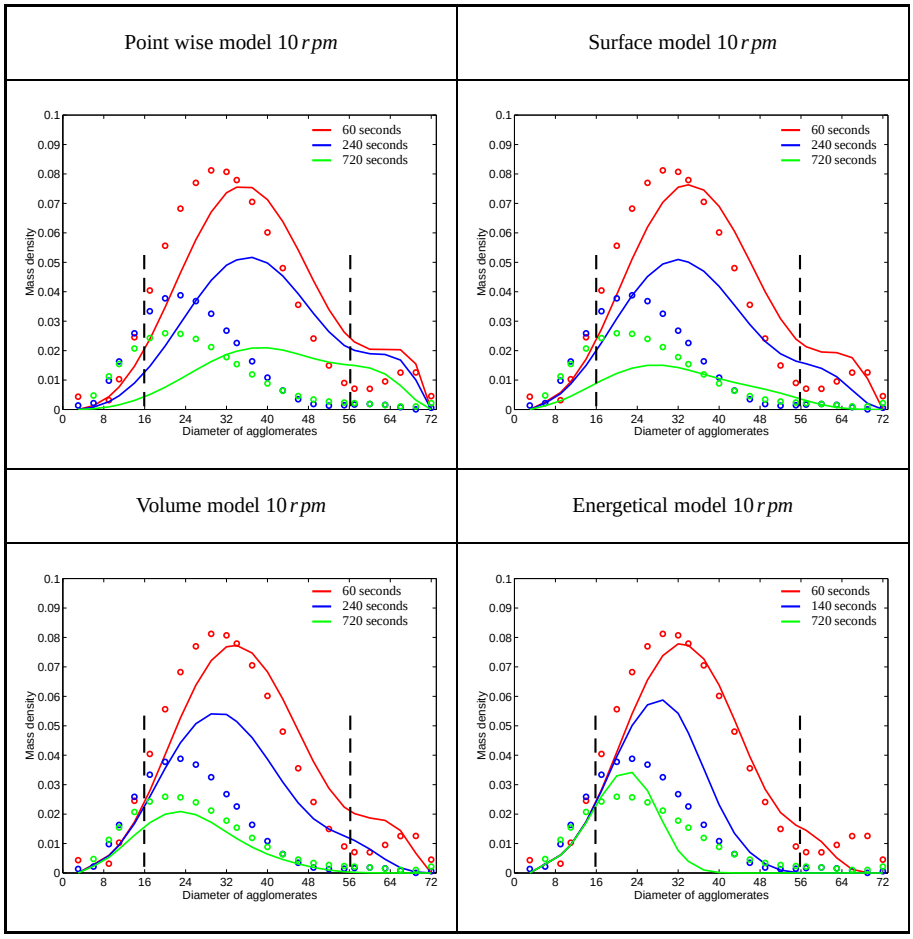

Figure 3.21: The mass fraction distributions predicted by the different continuous models at $10 rpm$ vs. the experimental mass fraction distributions. The values of κ, κ_1, κ_2 and κ_3 are equal to $11.25\,\frac{\mu m^3}{s}$, $1.15\,10^{-2}\,\frac{\mu m}{s}$, $6\,10^{-4}\,s^{-1}$ and $1.9\,10^{-6}\,\frac{1}{s\,\mu m}$.

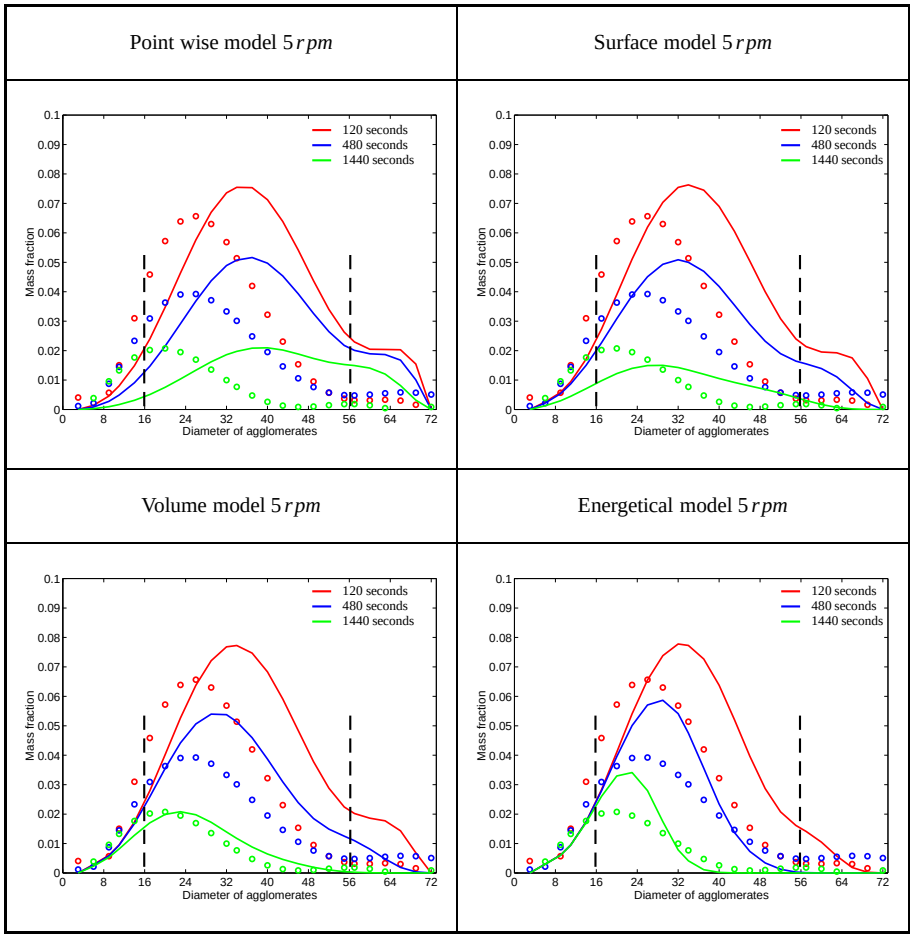

Figure 3.22: The mass fraction distributions predicted by the different continuous models at $5rpm$ vs. the experimental mass fraction distributions. The values of κ, κ_1, κ_2 and κ_3 are equal to $5.6\,\frac{\mu m^3}{s}$, $0.57\,10^{-2}\,\frac{\mu m}{s}$, $3\,10^{-4}\,s^{-1}$ and $9.9\,10^{-7}\,\frac{1}{s\,\mu m}$